Glass-ceramic sealant for solid oxide fuel cells application: characterization and performance in dual atmosphere

A. G. Sabato [1], G. Cempura [2], D. Montinaro [3], A. Chrysanthou [4], M. Salvo[1], E. Bernardo[5], M. Secco[6], F. Smeacetto* [1]

[1] *Department of Applied Science and Technology, Politecnico di Torino, Italy;*

[2] *AGH University of Science and Technology, Krakow, Poland;*

[3] *SOLIDPOWER SpA, Italy;*

[4] *School of Engineering and Technology, University of Hertfordshire, Hatfield, UK*

[5] *Department of Industrial Engineering, Universita' degli Studi di Padova, Italy*

[6] *Inter-Departmental Research Center for the Study of Cement Materials and Hydraulic Binders (CIRCe), Universita' degli Studi di Padova, Italy*

** Corresponding author: Federico Smeacetto, Politecnico di Torino, Corso Duca degli Abruzzi 24, 10129 Torino, Italy; e-mail federico.smeacetto@polito.it. Tel 0039 011 0904756 Fax: 0039 011 0904669*

Abstract

A glass-ceramic composition was designed and tested for use as a sealant in solid oxide fuel cell (SOFC) planar stack design. The crystallization behaviour was investigated by calculating the Avrami parameter (n) and the activation energy for crystallization (E_c) was obtained. The calculated values for n and E_c were 3 and 413.5 kJ/mol respectively. The results of thermal analyses indicate that this composition shows no overlap between the sintering and crystallization stages and thus an almost pore-free sealant can be deposited and sintered at 850 °C in air for 30 min. A gas tightness test has been carried out at 800 °C for 1100 hrs in dual atmosphere (Ar-H_2 and air) without recording any leakage. Morphological and crystalline phase analyses were conducted prior and following tests in dual atmospheres in order to assess the compatibility of the proposed sealant with the metallic interconnect.

1 Introduction

Solid oxide fuel cells (SOFCs) are promising devices for future clean energy production. These systems convert chemical energy into electrical energy by red-ox reactions between a fuel and an oxidant with very high efficiency. In order to reach a useful power output, it is necessary to connect in series several cells [1,2]. The planar stack design (where single cells are stacked one on top of each other and separated by a metallic interconnect) is easier to manufacture and leads to higher power density production in comparison to the tubular one [1,3,4]. One of the most important components in a planar stack is the sealant whose function is to prevent mixing of the reducing and oxidising gasses. The SOFC sealant is exposed to demanding conditions of high temperature 750-800 °C and both oxidizing and reducing atmospheres. A good sealant must be chemically and physically stable and be able to maintain a hermetic seal at the operating conditions for thousands of hours. Furthermore it must have good thermo-mechanical and thermo-chemical compatibility with materials to which it is in contact. In particular, maintaining a stable interfacial bond between the sealant and both the metallic interconnect (typically ferritic stainless steel) and the electrolyte (typically yttria stabilized zirconia) is critical [3,5,6]. The use of metallic brazes could provide a possible bonding solution, however, these can be expensive and have been reported to be unable to survive in the dual atmosphere present of the device [5,7]. Among the candidate sealants, glasses and glass-ceramics are likely to be the materials of preference as they exhibit better resistance to the severe service environment (oxidizing and reducing) than brazing alloys [8-14]. On the other hand compressive seals like mica-based seals can result in high leakage levels and it may be necessary to use them in combination with brazes or glass (for example infiltrating the glass into mica papers) [3,15]. Glass-ceramics offer the opportunity to tailor their properties by varying the composition and may also provide the potential of self-healing due to the presence of a remaining glassy phase. In order to maintain a hermetic seal, the glass-ceramic must be strongly bonded with the electrolyte and with the interconnect; it must also maintain a value of the coefficient of thermal expansion

(CTE) similar to those of the materials with which it is in contact. Such an approach will avoid crack formation and residual stresses during thermal cycling. Most of the research on glass-ceramic sealants has focused on BaO-containing glass-systems. The use of BaO tends to reduce the values of the glass transition temperature, T_g, and the glass softening temperature, T_s, while at the same time it increases the CTE value of the glass-ceramic. Depending on the glass composition, the formation of the monocelsian phase ($BaAl_2Si_2O_8$) which has a low value of thermal expansion (2-3 x 10^{-6} K^{-1}) is possible; however, the reaction of BaO at the interface with the steel along with the consequent formation of $BaCrO_4$ (with high CTE, around 20 x 10^{-6} K^{-1}) could lead to the detachment and spallation of the sealant. [6,9].

Bonding and sealing processes involving the use of glasses are usually carried out above the glass softening point, in order to achieve good densification as well as good wetting thanks to viscous flow; furthermore controlled devitrification can lead to the formation of crystalline phases that improve the thermomechanical properties of the glass-ceramic.

The aim of the work that is reported here is to develop a glass-ceramic system with excellent combination of properties including thermal stability and good sintering and densification behaviour that would effectively lead to a fully densified glass-ceramic at 850 °C. The sintering and crystallization behaviour as well as the thermal stability and compatibility between this sealant and a preoxidised steel have been examined. In addition, the ability of the glass-ceramic sealant to form and maintain gas tightness in dual atmosphere conditions for a period of up to 1100 hours has been investigated. Some groups have worked extensively on the diopside ($CaMgSi_2O_6$) system. Much of this work has been driven by the research group of Ferreira [16] who have produced detailed studies on a number of diopside-based glass systems including rare-earth and strontium-containing aluminosilicate glass ceramic sealants. Reddy et al [17] also studied the effect of strontium-to-calcium ratio on the structure, the crystallization behavior and properties of diopside-based glasses. These investigations on diopside systems have yielded promising results for use as sealants in SOFC applications [18]. The work which is reported here

has considered the addition of sodium oxide in diopside owing to its lower cost and its possible benefits with regard to ease of processing.

The possibility of adverse effects in the presence of alkaline-earth metal oxides in sealing glasses for SOFC applications is discussed in Chou et al [19] who observed detachment of the sealant due to the formation of alkaline-earth chromates (i. e. BaCrO4 and SrCrO4). The same glass was used as a sealant for aluminized Crofer22APU and in this case the alumina layer on the steel dissolved, suggesting that the presence of alkalis in the sealing glass made the glass more corrosive than alkali-free glass. In another study [20], a glass containing about 17 mole% alkali metal oxides (K_2O and Na_2O) was used in contact with an aluminized SS441 substrate; isothermal ageing in dual environment exhibited good hermetic behaviour during a test that was conducted for 1000 h. The glass was found to be compatible with the alumina coating since no adverse reactions were detected.

In the present study, a glass-ceramic composition was therefore specially formulated expecting a reduction in the characteristic temperatures leading to processing benefits. The possibility of formation of sodium chromate is a concern and as result other groups have so far not considered the use of sodium in diopside systems. However, when working on alternative glass-ceramic systems, the present authors [11, 14] previously showed that such problems may be overcome by tailor-making compositions where sodium was able to diffuse away from the sealant-interconnect interface and thus prevent any undesirable effects.

2 Experimental

2.1 Glass and glass-ceramic characterization

A glass with the composition reported in Table 1, has been designed using data from the SciGlass® database (Science Serve GmbH, SciGlass 6.6 software, Newton, MA, USA). The glass, labelled V9, was produced by melting in a furnace the raw materials (carbonates and oxides) at 1600°C for 1 h in a Pt-Rh crucible.

Chemical composition (wt%)						
Oxide	Starting glass V9	V9 glass-ceramic 850 °C 30 min air		V9 glass-ceramic 800 °C 1100 hrs dual atm.		
		Crystal phase 1	Residual glass phase	Crystal phase 1	Crystal phase 2	Residual glass phase
SiO_2	50.4	47.1	52.1	55.5	68.7	41.1
Al_2O_3	8.3	14.1	5.4		19.5	11.1
CaO	9.3	25.9	0.9	25.9		
MgO	13.0	12.9	13.0	18.6		12.8
Na_2O	10.3		15.5		11.8	17.3
ZrO_2	2.9		4.4			6.0
B_2O_3	5.8		8.7			11.7
Phase distribution (wt%)						
Diopside		33.9 $[CaMg_{0.7}Al_{0.6}Si_{1.7}O_6]$		36.1 $[CaMgSi_2O_6]$		
Albite					14.9 $[NaAlSi_3O_8]$	
Glass	100		66.1			49.0

Table 1. Composition of V9 glass (wt.% of oxides), composition (wt.% of oxides) and relative amount of amorphous and crystalline phases in the glass-ceramic after the joining process (850°C, 30 min in air) and after the gas tightness test (800°C, 1100 hours, dual atmosphere), obtained by Rietveld refinement.

The molten glass was quenched by casting onto a brass plate. The V9 glass was then ground using a zirconia ball mill and subsequently sieved. Differential thermal analyses (DTA) (Netzsch, Eos, Selb, Germany) were conducted on glass powders with three different particle sizes (< 25 µm, 25-38 µm, and 38-63 µm) at a heating rate of 5 °C/min from room temperature to 1300 °C.

Hot-stage microscopic analysis (HSM) (Expert System Solution, Modena, Italy) was recorded at 5 °C/min on compacted V9 glass powders of particle size <25 µm to determine the characteristic temperatures of the glass and its sintering behaviour. The DTA and HSM results were used to select the thermal treatment for the formation of the glass-ceramic and the sealing process as used in the investigation. The selected conditions were a thermal treatment at 850°C for 30 min in air and heating rate of 5°C/min. Additional DTA analyses at different heating rates (10/20/30/40 °C/min) were carried out in order to study the crystallization behaviour of the glass-ceramic system.

Dilatometry (DIL) (Netzsch, DIL 402 PC/4) was performed at a heating rate of 5 °C/min for the as-cast V9 glass, the V9 glass-ceramic in order to evaluate the coefficient of thermal expansion, CTE, and the dilatometric softening temperature (T_s) before and after the devitrification process (heat treatment at 850°C, 30 min, air) and after the dual atm test at 800°C for 1100 hrs. The dilatometric measurements were conducted using cylindrical samples of diameter 4mm and height of around 5 mm (for as cast before and after the devitrification process samples) and on a small glass-ceramic bar (5 mm length) for the sample after 1100 hrs at 800°C

Three samples were used to determine the glass transition temperature ; T_g was taken at the onset, obtained by the intersection of the two tangents at the start of the endotherm. Three samples were used for determination of the mean CTE value and the error was $\pm$ 0.16 x 10^{-6} K^{-1}.

The glass-ceramic was subjected to chemical and morphological analyses using scanning electron microscopy (SEM) and energy dispersive X-ray spectroscopy (EDS) (using Merlin microscope of ZEISS). The samples were prepared for these analyses by polishing using SiC paper. The crystalline phases were studied by means of X-ray diffraction on powdered samples (XRD; Bruker AXS D8 Advance, Bruker, Germany). A semi-automatic phase identification was performed by means of the Match! Program package (Crystal Impact GbR, Bonn, Germany) supported by data from PDF-2 ICDD-International Centre for Diffraction Data, Newtown Square, PA and by the Crystallography Open Database. Mineralogical quantitative phase analysis

(QPA), based on the Rietveld method, was performed using the TOPAS software (Bruker AXS, Karlsruhe, Germany). The contents of crystalline and amorphous phases were determined using the combined Rietveld-RIR method, using 20 wt% of zincite as internal standard. The observed patterns were modelled through a pseudo-Voigt function, fitting the background by 14 Chebyshev polynomials [21]. For each phase, the lattice parameters, Lorentzian crystal sizes and scale factors were refined and residual preferred orientation effects were modelled with the March Dollase algorithm [22]. The XRD analysis after the dual atm tests at 800°C for 1100 hrs has been carried out on the powdered glass-ceramic recovered after disassembling the 441/V9/441 joined structure and mechanically removing the glass-ceramic.

2.2 Joined samples and gas tightness test

The joining between the glass-ceramic and the preoxidised 441 stainless steel (preoxidation at 870°C, 3 hrs in air) was carried out by manually depositing a slurry PVB-based paste (solid load: 77wt%) of glass powders (<25µm) and ethanol between two 441 stainless steel coupons. The CTE value of the 441 stainless steel is 12.8 x 10^{-6} K-1 (T range 20-800°C). These samples were heat treated at 850°C for 30 minutes in air at a heating rate of 5°C/min in order to obtain a good degree of sintering and densification, as well as a consistent amount of crystalline phases. “Sandwich-like” samples of the sequence preoxidized steel/V9 glass-ceramic/preoxidized-steel were subjected to a gas tightness test in dual atmosphere using static air on one side and fluxed N_2/H_2 50 vol% on the other at 800 °C for up to 1100 hrs in order to check for the presence of gas leakage .

SEM/EDS analyses were carried out prior and after the test in dual atmosphere. Analyses using XRD, SEM/EDS, transmission electron microscopy (TEM) and selected area electron diffraction (SAED) were also carried out in order to check for changes in the nature and amounts of the crystalline phases following exposure under the various conditions stated above. Specimens for TEM investigations (BF, DF, SAED), were prepared, using FIB (Focus Ion Beam) technique on NEON CrossBeam 40EsB of ZEIratSS.

3 Results and discussion

3.1 Glass characterization

Fig. 1a shows the effect of the heating rate on the glass transition temperature (Tg) and the crystallization peak temperature (T_p) of the V9 powder of less than 25 μm, while the effect of powder size at a constant heating rate of 5 °C/min is presented in fig. 1b. For the V9 sample, the values of the T_g and T_m were observed to be 600 °C and 1176 °C, respectively, while the onset of crystallisation was located at a temperature, T_x, of 820°C. Fig.1a shows a shift in the value of T_c and T_p to higher temperatures with increasing heating rate for powders of size < 25 μm. An indication of the thermal stability of glasses may be obtained by the Hruby parameter which is defined as $(T_x - T_g)/(T_m - T_x)$ [23]. The thermal stability criterion of $T_x - T_g$ was introduced by Dietzel [24]. For the V9 composition, the difference between the two temperatures is 230 °C which is relatively high and thus there will be a delay in the onset of nucleation as the composition is heated up. This suggests that the glass-ceramic is likely to be thermally stable which is good from the point of view of developing this glass-ceramic composition as a sealant for SOFC applications. Comparing these data with results reported by Goel et al [16] who thermally characterised various diopside compositions (without any sodium in the glass) shows that the the proposed composition in the current investigation has widened the difference between the T_x and T_g values suggesting an increase in the thermal stability; the onset of the endotherm was experimentally used to obtain the Tg values in both the cases. A wider temperature range between the T_x and T_g values may be attractive because it extends the range where viscous flow and self-healing may take place.

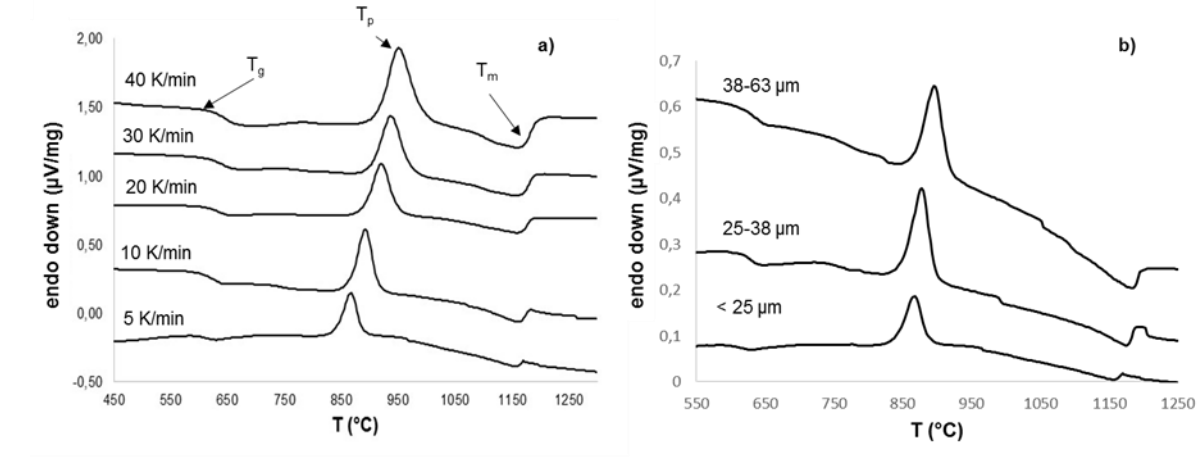

Figure 1**.** DTA plots of V9 powders: < 25 µm at different heating rates (a) and at 5 °C/min on different powders sizes (b).

The activation energy for crystallization (E_{ck}) can be calculated, using the Kissinger equation (eq.1), from the variation of T_p with the heating rate (α) [25] and was found to be 268.6 kJ/mol:

$$Ln\left(\frac{\alpha}{T_P^2}\right) = -\frac{E_{cK}}{RT_P} + cost. \qquad (1)$$

Matusita and Sakka [26] reported that eq.1 can be used only if the crystallization mechanism is completely by surface growth. In the other cases, Matusita and Sakka equation (eq.2) should be used:

$$Ln\left(\frac{\alpha^n}{T_P^2}\right) = -\frac{mE_c}{RT_P} + cost. \qquad (2)$$

where *n* is the Avrami parameter (related to the mechanism of growth), *m* is the dimensionality of growth of the crystalline phase and E_c is the activation energy for crystallization. If the mechanism of growth is surface crystallization, both *n* and *m* are equal to 1 and eq.2 becomes equal to the Kissinger equation. By using the Ozawa equation (eq.3), it is possible to obtain the value of *n* from DTA measurements taking into account the variation of volume fraction of the crystallized phase (χ) with the heating rate at a fixed temperature T [27].

$$n = -\left(\frac{d\{ln[-ln(1-\chi)]\}}{d(ln\alpha)}\right)_T \qquad (3)$$

The value of χ has been evaluated from DTA crystallization peaks as the ratio between the partial area under the peak at the chosen temperature and the total area under the peak. The

value of n was calculated by evaluating the slope of Ozawa plots (ln[-ln(1-χ)] vs. lnα) at four different fixed temperatures (905°C, 910°C, 915°C, 920°C) using four different heating rates (10°C/min, 20°C/min, 30°C/min, 40°C/min) for each temperature (Ozawa plots not shown here). The value of n was calculated as the average of the four values obtained as described above and is equal to 3, a value that would suggest the bulk crystallization mechanism [28] to be active. Assuming that the number of nuclei is not constant, by varying the heating rate (m = n - 1), m = 2 and bi-dimensional growth would be expected [28-33]. It is possible to obtain E_c, with these two values, from the slope of the Matusita and Sakka plot (Fig.2). Table 2 presents the calculated kinetic parameters and activation energies for the crystallization (E_{cK} and E_c) of V9 glass powders (< 25 μm).

A value of 3 for the Avrami parameter would indicate bulk crystallization. This may be in contrast with the shift in the T_g and T_p peaks as the powder size varied; fig 1b indicates that the number of the crystallization nuclei changes varying the extent of the specific surface (i. e. the dimension of the particles); the increase of T_p (867°C, 883°C, 896°C) is substantial considering the small difference in the powder size. In the case of bulk crystallization different results would be expected since the lower the particle size the greater the tendency to devitrification by nucleation and growth from surface nuclei.

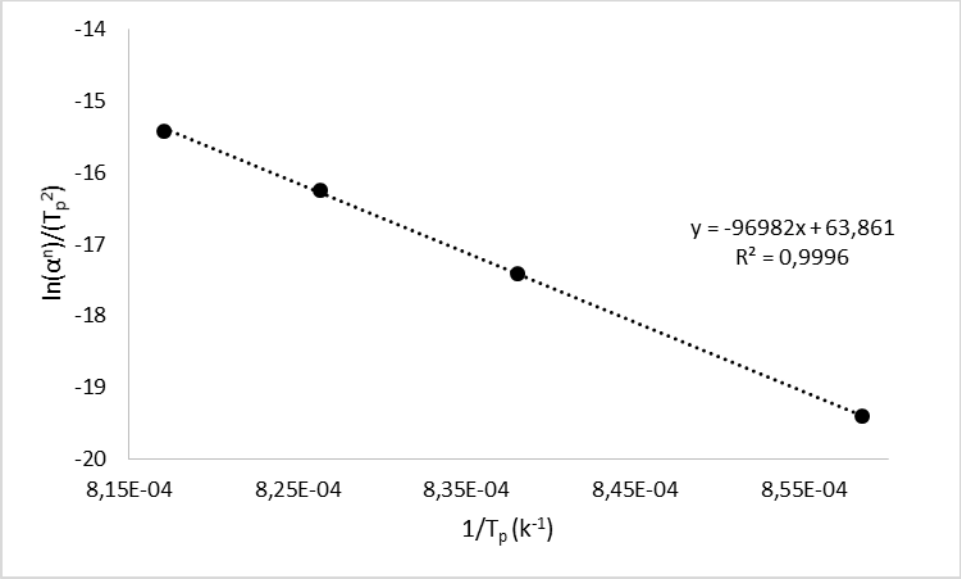

Figure 2. Matusita and Sakka plot for V9 powders (< 25 μm).

E_{ck} (kJ/mol)	n	m	E_c (kJ/mol)	mE_c (kJ/mol)	nE_{ck} (kJ/mol)
268.6	3	2	413.5	806.4	792.2

Table 2. Kinetic parameters (n and m) and activation energies for crystallization obtained by Kissinger equation (E_{cK}) and Matusita and Sakka equation (E_c), for V9 powders (< 25 μm).

The same trend was previously observed for similar glassy systems [31-33] where effective sintering of the glass by viscous flow occurs prior to crystal growth. In these systems, nuclei that formed on surface sites can act as bulk nuclei during growth following the sintering stage, thus explaining the consistency of the DTA results and the calculated kinetics parameters [29-31]. The reason of this "contradiction" is that the nuclei are formed on the surface of the particles at a temperature between T_g and T_x, prior to sintering by viscous flow. These nuclei act as bulk nuclei after the sintering and during crystal growth.

In Table 2 the values of mE_c and nE_{cK} are shown to be very close to each other and a difference less than 2%. This observation is in agreement with the work of Erol *et al* [33] who suggested that the values of nE_{ck} and mE_c can be considered similar and approximately within 10% of each other.

The determination of the correct order of events is very important in order to derive the conditions for optimum densification of the sealant during the joining process as viscous flow sintering and crystallization are two competitive phenomena; while the viscosity of a glass decreases with increasing temperature promoting densification, the viscosity of a glass with crystalline inclusions may be significantly enhanced with increasing degree of crystallization leading to the effect of "freezing" the densification [34].

The activation energy is an indication of the rate of the crystallization and the Avrami parameter is related to the crystallization mechanism, while HSM and DTA data provide details of the sequence of events. Since crystallization can reduce the rate of densification it is important to have knowledge of the sintering and crystallization kinetics in order to derive the optimum heat-treatment schedule for the production of glass-ceramic sealants from powders by the sintering-crystallization method. The joining heat-treatment process usually requires a low heating rate

(5K/min or less) and it is fundamental to manage the correct order of events, thus avoiding excessive crystallization that may obstruct viscous flow.

Fig.3 depicts the superimposition of HSM and DTA curves (together with characteristic temperatures) recorded at a heating rate of 5 °C/min for V9 glass powders with particle size < 25 µm. From the HSM analysis, the maximum shrinkage temperature (T_{ms}) has been observed to occur at 750 °C, while at higher T the change of the slope until 850°C is due to viscous flow. In the view of this, the difference between T_x and T_{MS} was found to be 70 °C, thus supporting that this systems exhibits a very good sintering ability.

Considering the occurrence of significant viscous flow at 850 °C, we expected good densification at this temperature by treating for 30 min in air. Dilatometry was carried out both for pellets of the as-cast V9 glass and the V9 glass-ceramic (V9 heat treated at 850°C, 30 min, air). The recorded CTE values were 7.55 * 10^{-6} K^{-1} and 9.52 * 10^{-6} K^{-1} (300-550 °C), respectively for the V9 glass and the V9 glass-ceramic.

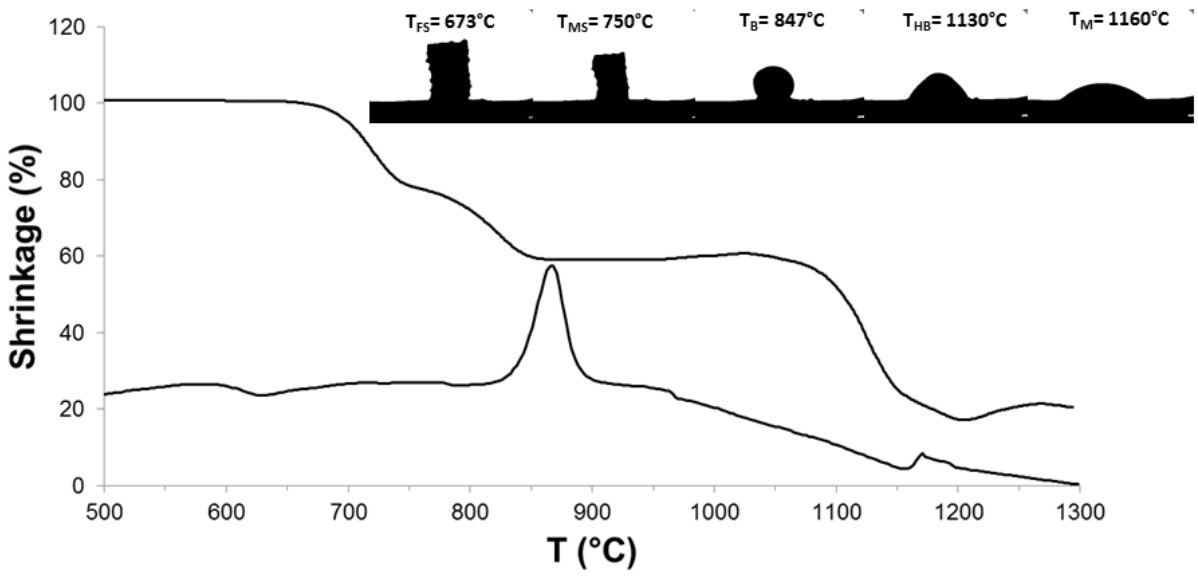

Figure 3. HSM and DTA of V9 powders (< 25 µm) recorded at 5 °C/min

3.2 Joined samples, gas tightness test in dual atmosphere and post mortem analyses

Morphological analyses of the samples following the sealing/joining process showed good interfacial bonding between the glass-ceramic and the preoxidised 441 steel (Fig. 4). A uniform

preoxidation layer (thickness of around 1 micron) is present at the interface between the sealant and the 441 steel. As expected from the study of the V9 sintering behaviour (section 3.1) and the similar CTEs of V9 and 441 steel, the sealant, as predicted by the results of the initial characterisation, exhibited no cracks and contained only minor levels of porosity. In addition, very good adhesion was observed between the glass-ceramic and the preoxidised steel. The SEM micrograph in Fig. 4 shows the crystalline phases (the brightest areas) formed during the thermal treatment with a considerable amount of the glassy phase (the darkest areas) remaining. One of the advantages of having a glassy phase present is its ability for self-healing in case of damage. Fig. 4 shows the presence of a layer of diopside crystals along the interface between the preoxidised 441 stainless steel and the sealant. The fact that these crystals that are of smaller size than those in the bulk of the sealant and are densely populated at the interface with the interconnect, implies that they were formed by heterogeneous nucleation on the 441 stainless steel surface. The resulting diopside layer has thickness of about 3 μm and shields the Cr2O3 preoxidised layer from the Na2O which is present in the remaining glass phase.

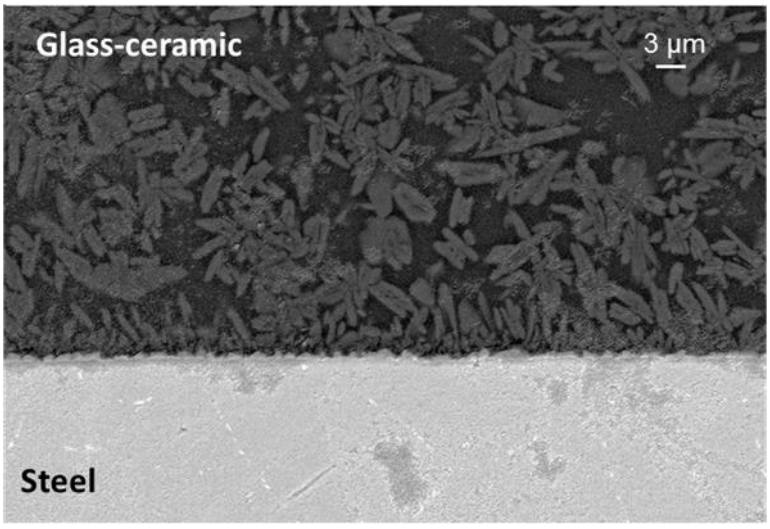

Figure 4. FE-SEM image (back-scattered electrons) of the interface between the V9 glass-ceramic and the preoxidised 441 steel, after the joining process at 850 °C for 30 min in air.

The V9 sealant fuel leakage was measured by closing the gas outlet and measuring the minimum H_2 flow rate needed to reach an overpressure of 10 mbar. The leakage observed by

this technique during the hermeticity test for up to 1100 hrs at 800 °C was below the detection limit of 1 ml/min.

SEM and EDS maps from different regions of the steel/glass-ceramic interface following exposure to the dual atmosphere are presented in figures 5 and 6 respectively. The SEM examination reported in Fig. 5 showed that the preoxidized steel and the glass-ceramic sealant interface remained well-bonded and still sound and was free of cracks without evidence of sealant detachment or spallation. In these areas the glass-ceramic maintained good adhesion with the steel (Fig.5a); EDS elemental maps show that there was no elemental diffusion between the glass-ceramic and the steel. The formation of a Cr-rich oxide scale at the interface is evident along with a non-uniform layer containing Ti, Cr, Fe, Si and O being visible just below the interface.

It was also observed that diopside grains nucleated heterogeneously at the surface of the stainless steel as shown in fig. 4 and effectively created a diopside layer that shielded the chromium oxide from the glass phase (that contains the sodium) during the test. In Fig. 6 there is evidence of corrosion of the steel at the interface with the sealant. Previous investigations [35] on the effect of exposure in dual atmospheres have reported that oxidation of the interconnect lying on the air side may take place.

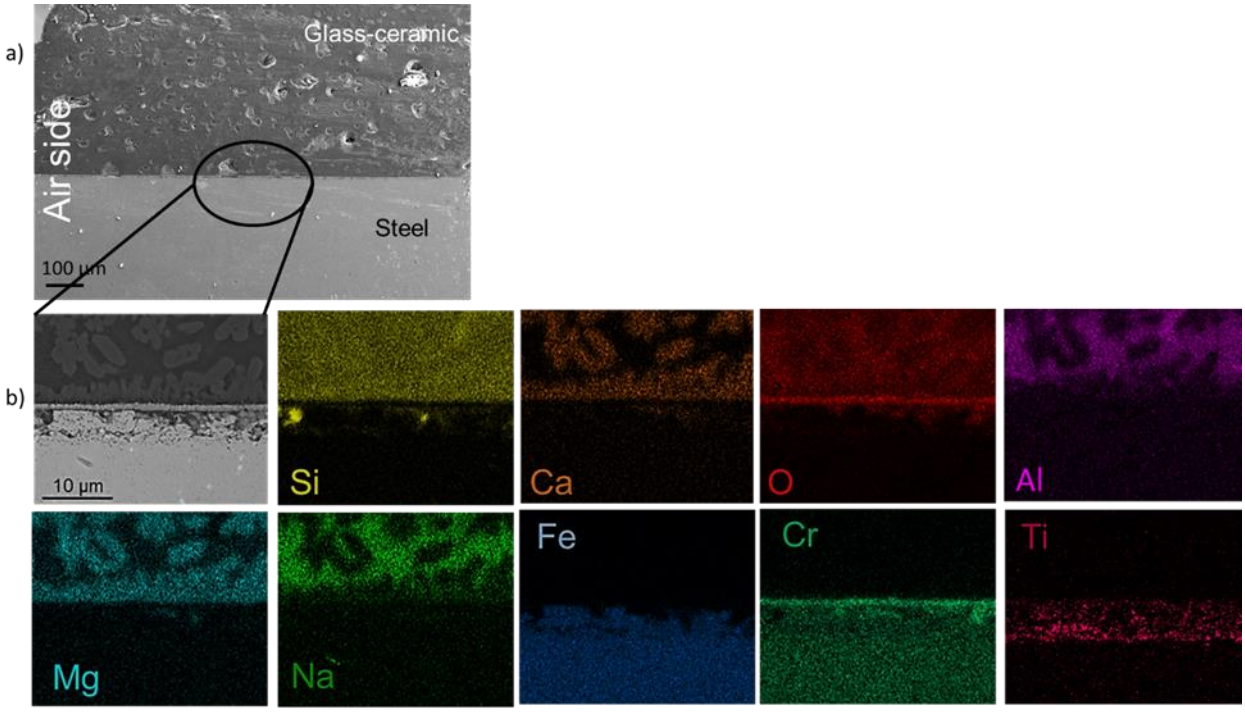

Figure 5. FE-SEM image (secondary electrons) (a) and EDS maps (b) of the interface V9 glass-ceramic/preoxidised 441 steel after the dual atmosphere test, collected at the air side.

The EDS analysis shows the presence of a thin protective Cr_2O_3 layer at the interfacial areas where there was good contact between the glass-ceramic sealant and the stainless steel interconnect, while breakaway corrosion is evident in an area where there was no contact between the two materials. Closer observation of the corroded area revealed a void just above the steel. This suggested that this void had been formed during the sealing procedure. Formation of this type of void is unlikely to have formed by vaporisation of chromium because the EDS analysis does not show any chromium depletion in the alloy. The corroded area was divided into two parts; the lower part was rich in iron, chromium and oxygen and appeared to be a spinel, while in the upper part only iron and oxygen were detected suggesting the formation of either Fe_3O_4 or Fe_2O_3. A crack ran through the corroded part separating the iron oxide from the spinel. A thin chromium oxide-rich layer was observed at the interface between the iron oxide layer and the spinel phase.

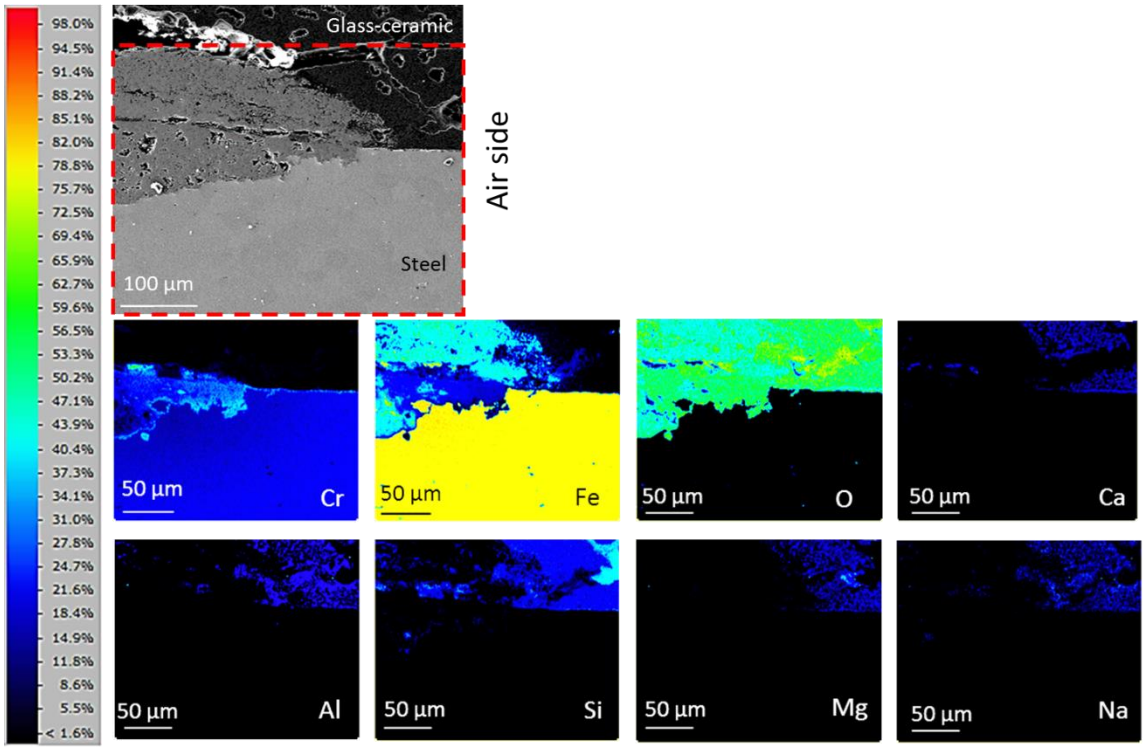

Figure 6. FE-SEM image and EDS maps of the V9 glass-ceramic/preoxidised 441 steel collected at the air side. The EDS maps are inherent to the marked area in the image on the top. The reported scale is wt. %.

The chromium oxide-rich layer was probably the original layer produced by pre-oxidation, though in some areas there appeared to be further chromium oxide enrichment just above the original Cr_2O_3. A thin Cr_2O_3 layer was also evident at the interface between the spinel phase and the underlying stainless steel. The observed corrosion behavior was probably dictated by the partial pressure of oxygen at the stainless steel surface. At the area where the steel was bonded to the glass-ceramic sealant, the latter provided protection from oxidation by shielding the steel. As a result, the partial pressure of oxygen at the interface was very low and this prevented any severe oxidation from taking place. On the other hand, within the void at the edge of the sample, there was either trapped air or direct access of air to the stainless steel. According to Amendola [36] and Bram [37] pre-oxidation of stainless steel for at least 100 hrs at 800°C is necessary to suppress breakaway corrosion in a dual-phase atmosphere. The steel in the current study had been pre-oxidised for a far shorter time and prolonged exposure to air led to oxidation of both iron and chromium. The observed corrosion involved the outward diffusion of iron to form the external iron oxide product. As the iron diffused outwards, voids were created in the underlying

regions (within the spinel phase). On the other hand, the mechanism of the spinel formation involved the diffusion of oxygen into the alloy. At the interface between the stainless steel and the spinel, a thin Cr_2O_3 layer was formed and this is in agreement with chemical thermodynamic calculations that suggest that the inner oxide should be the one that forms at the lower partial pressure of oxygen. The outer oxidised layer was composed entirely of iron oxides which do not adhere well onto the surface of stainless steel. Thus a crack was observed running through the oxidised area separating the iron oxides from the spinel. Spallation of the iron oxides is likely to occur with time. Another possible risk related to the presence of Fe oxide could be the short-circuiting by connection of contiguous interconnect plates. On the positive side, there was no chromium depletion in the underlying area and therefore the spinel layer would be expected to provide protection after spallation of the iron oxides in the upper part. The EDS elemental maps have shown that no elements from the sealant are present in the corroded region. This observation can exclude the possibility of interaction between the steel and the sealant. Moreover other SEM images (not reported here) show that the beginning of the corrosion is between the Cr containing scale and the bulk of the steel, with a consistent volume increase that lead to the break of the scale, as well as the presence in some regions of internal corrosion along grain boundaries within the steel.

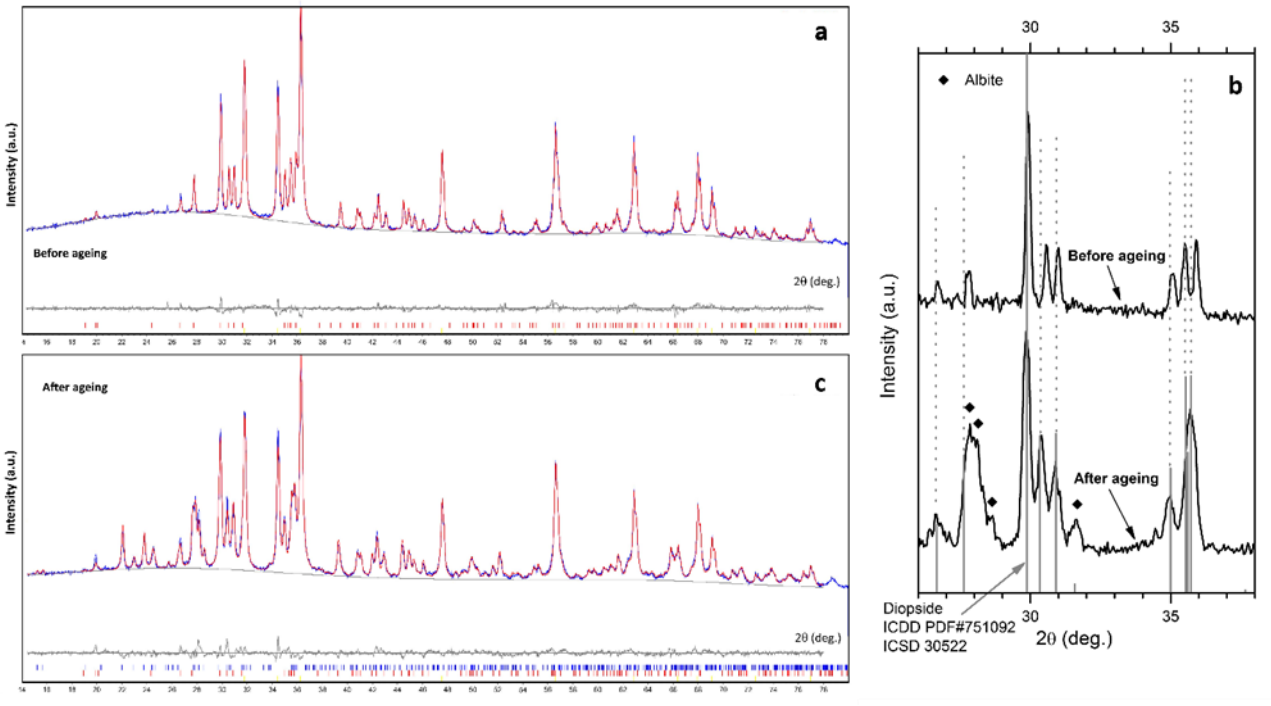

Figure 7. XRD powders analysis of V9 glass-ceramic: a) pattern of sample after the joining process (850°C, 30 min, air); b) comparison of experimental patterns with that of pure diopside; c) pattern of sample after the tightness test (800°C, 1100 hours, dual atmosphere).

XRD analyses of the glass-ceramics, illustrated by Fig.7, were carried out in order to investigate the nature and the amount of the crystalline phases present after the joining process and after the test in dual atmosphere. After the joining process, the pattern featured a visibly large amorphous halo (see Fig.7a) as proof of limited crystallization, while the peaks did not match well with those of pure diopside ($CaMgSi_2O_6$, ICSD 30522) (see Fig.7b). Good refinement of experimental data (blue lines in Fig.7a) was found with an Al-containing diopside solid solution ($CaMg_{0.7}Al_{0.6}Si_{1.7}O_6$, COD 96-900-5278; the detected crystal phase corresponds to the formula $CaMg_{1-x}Al_{2x}Si_{2-x}O_6$, with x=0.3, whereas pure diopside obviously corresponds to x=0). Following exposure to the dual atmosphere, the amorphous halo decreased (Fig.7c) and two different crystalline phases could be detected. In fact, the major peaks now correspond to those of pure diopside (that contains no aluminium, see Fig.7b), while albite, i.e. a sodium feldspar ($NaAlSi_3O_8$, COD 98-004-6398) has also appeared. The EDS and XRD analyses had shown the crystallization of the Al-containing diopside solid solution ($CaMg_{0.7}Al_{0.6}Si_{1.7}O_6$) during the joining stage. The formation of albite occurred during the testing of the sealant and is associated with the diffusion of aluminium away from the diopside along with reaction with the glass. By using the Rietveld method, quantitative data were obtained by refinement of the diffraction patterns by mixing the V9 glass-ceramic powders with an internal standard (zincite powders). The results are presented in Table 1. The reduction of the amount of the amorphous phase from 66% to 49%, after prolonged heating at 800 °C, can be correlated to the appearance of albite; the Al^{3+} ions, originally present in the diopside solid solution, diffused out, being mostly incorporated in the feldspar phase; However, despite the formation of albite, the CTE of the glass-ceramic sample after 1100 hrs at 800°c was found to be 9.6 x 10^{-6} K^{-1} .. The presence of “un-doped” diopside in the aged sample was confirmed by the SAED analyses. Two different electron diffraction patterns were collected from two different crystals from the V9 glass-ceramic after FIB thin

lamella preparation; in both cases, good matching with the electron diffraction pattern of pure diopside was observed (Fig.8).

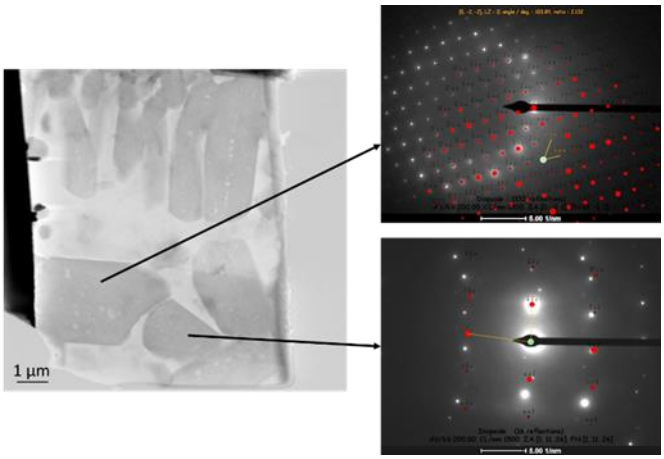

Figure 8. TEM and SAED indexed analysis from two different crystals of the V9 glass-ceramic after dual atm tests, at 800°C for 1100 hrs.

While the diopside composition changes with time by the loss of aluminium, it is evident that the altered diopside phase remained in good contact with the 441 stainless steel interface. The EDS and XRD analyses following testing for 1100 hrs, indicated that the crystalline phase at this area was diopside which contained Ca, Mg, Si and O and presented a barrier to the sodium-containing phases. This is of great interest with regard to the use of the glass-ceramic for use as a sealant for SOFC applications because this behaviour can prevent contact between the sodium and Cr_2O_3 and effectively avoid formation of sodium chromate which is undesirable.

The V9 glass-ceramic composition that was used in this investigation was specially formulated by taking into consideration the fact that alkali metals may lead to a decrease of the characteristic temperatures and thus may improve or enable glass flow at lower temperatures. It is also expected that this will improve the wettability of glasses with the 441 stainless steel and provide good CTE matching. This particular composition was chosen for its excellent sintering and densification behavior at a deposition temperature of 850°C and for the use in SOFC real conditions (i.e. dual atm tests) at 800°C.

The XRD analysis showed the presence of only diopside, the residual glassy phase and albite and no evidence of sodium chromate and therefore it was concluded that there was no deleterious interaction between the steel and the sealant.

4 Conclusions

A barium-free glass-ceramic composition based on diopside has been designed for use as a sealant in SOFCs planar stacks. Its crystallization behaviour has been investigated by means of HSM and DTA analyses in order to calculate the Avrami parameter (n) and activation energy for crystallization. The results showed a value of n equal to 3 which suggests that crystallization occurs predominantly from the bulk. This could be explained by considering that the nuclei formed on the surface act as bulk nuclei following effective sintering by viscous flow especially if we consider that there is only a slight overlap between sintering and crystallization. Following the joining process, the crystallized phase was identified to be Al-containing diopside. Microscopic analysis showed evidence of nucleation of diopside grains on the surface of the stainless steel. These heterogeneously nucleated diopside grains separated the sodium-containing glass phase from the stainless steel thus preventing the formation of undesirable sodium chromate. The presence of albite, in addition to diopside was observed after the dual atm tightness test for 1100 hrs at 800 °C. The results of Rietveld refinement showed that the amount of the amorphous phase slightly decreased during the test; this observation coincided with the formation of albite and a slight increase in the amount of diopside. The glass-ceramic shows good densification after the sintering process at 850 °C for 30 min in air as well as thermo-chemical and thermo-mechanical compatibility with the pre-oxidised stainless steel. Gas tightness tests that were performed over a period of 1100 hrs at 800°C showed no evidence of any leakage.

The observed corrosion involved the outward diffusion of iron to form the external iron oxide product. Since no elements from the sealant are present in the corroded region, the possibility of interaction between the steel and the sealant is excluded.

The main risk associated to corrosion near the seal is the formation of Fe oxide that could reduce the life time and the efficiency of a potential stack. A follow up of this study will involve a similar test on a coated steel with the specific purpose to avoid such corrosion phenomena.

Acknowledgments

The research leading to these results has received funding from the European Union Seventh Framework Programme under Grant Agreement 312483 - ESTEEM2 (Integrated Infrastructure Initiative–I3).

The KMM-VIN Research Fellowship (6th call) for the research stay of A. G. Sabato at AGH, Krakow is also acknowledged.

References

[1] EG&G Technical service, Inc. Fuel cells handbook, seventh ed., U.S. Department of Energy, Office of Fossil Energy, National Energy Technology Laboratory, Morgantown, West Virginia, 2004.

[2] S.C. Shingal, K. Kendall, High temperature solid oxides fuel cells: fundamental, design and application, first ed., Elsevier Ltd, London, 2003.

[3] N. Mahato, A. Banerjee, A. Gupta, S. Omar, K. Balani, Progress in Material Selection for Solid Oxide Fuel Cell Technology: A Review, Progr. Mat. Sci. 72 (2015), 141-337.

[4] S.C. Shingal, Solid oxide fuel cells for stationary, mobile, and military applications, Solid State Ionics 152-153 (2002), 405-410.

[5] N. Singh, Sealing technology for SOFCs, Int. J. Appl. Ceram. Technol. 4 (2007), 134-144.

[6] J.W. Fergus, Sealants for solid oxide fuel cells, J. Power Sources 147 (2005), 46-57.

[7] Y.S. Chou, J.W. Stevenson, Novel silver/mica multilayer compressive seals for solid oxide fuel cells: The effect of thermal cycling and material degradation on leak behaviour, J. Mater. Res. 18 (2003), 2243-2250.

[8] M.K. Mahapatra, K. Lu, Seal glass for solid oxide fuel cells, J. Power Sources 195 (2010), 7129-7139.

[9] D.U. Tulyaganov, A.A. Reddy, V.V. Kharton, J.M.F. Ferreira, Alluminosilicate-based sealants for SOFCs and other electrochemical applications- A brief review, J. Power Sources 242 (2013), 486-502.

[10] F. Smeacetto, M. Salvo, M. Ferraris, J. Cho, A. R. Boccaccini, Glass–ceramic seal to join Crofer 22 APU alloy to YSZ ceramic in planar SOFCs, J. Eur. Ceram. Soc. 28 (2008), 61-68.

[11] F. Smeacetto, A. De Miranda, A. Chrysanthou, E. Bernardo, M. Secco, M. Bindi, M. Salvo, A.G. Sabato, M. Ferraris, Novel glass-ceramic composition as sealant for SOFCs, J. Am. Ceram. Soc. 97 (2014), 3835-3842.

[12] M.O. Naylor, T. Jin, J.E. Shelby, S.T. Misture, Galliosilicate glasses for viscous sealants in solid oxide fuel cell stacks: Part I: Compositional design, Int. J. Hydrogen Energy 38 (2013), 16300-16307.

[13] A.A. Reddy, N. Eghtesadi, D.U. Tulyaganov, M.J. Pascual, L.F. Santos, S. Rajesh, F.M.B. Marquesa, J.M.F. Ferreira, Bi-layer glass-ceramic sealant for solid oxide fuel cells, J. Eur. Ceram. Soc. 34 (2014), 1449-1455.

[14] F. Smeacetto, A. Chrysanthou, T. Moskalewicz, M. Salvo, Thermal cycling of Crofer22APU-sealant-anode supported electrolyte joined structures for planar SOFCs up to 3000 h, Mater. Lett. 111 (2013), 143-146.

[15] S.P. Simmer, J.W. Stevenson, Compressive mica seals for SOFC applications, J. Power Sources 102 (2001), 310-316.

[16] A. Goel, E.R. Shaaban, D.U. Tulyaganov, J. M. F. Ferreira, Study of crystallisation kinetics in glasses along the diopside-Ca-Tschermak join, J. Am. Ceram. Soc. 91 (2008), 2690-2697

[17] A. A. Reddy, D. U. Tulyaganov, G. C. Mather, M. J. Pascual , V. V. Kharton, S. I. Bredikhin, V. A. Kolotygin, J. M. F. Ferreira, Effect of strontium-to-calcium ratio on the structure, crystallization behavior and functional properties of diopside-based glasses Int. J. Hydrogen Energy 39 (2014), 3552-3563.

[18] A. A. Reddy, A. Goel, D. U. Tulyaganov, M. Sardo, L. Mafra, M. J. Pascual, V. V. Kharton, E. V. Tsipis, V. A. Kolotygin, J. M. F. Ferreira, Thermal and mechanical stability of lanthanide-containing glass–ceramic sealants for solid oxide fuel cells, J. Mater. Chem. A (2014), 1834-1846.

[19] Y. S. Chou, J. W. Stevenson, Jung-Pyung Choi, Alkali effect on the electrical stability of solid oxide fuel cell sealing glass, J. Electrochem. Soc. 157 [3] (2010) B348 - B353

[20] Y. S. Chou, E.C. Thomsen, R.T. Williams, J.-P. Choi, N.L. Canfield, J.F. Bonnetta, J.W. Stevenson, A. Shyam, E. Lara-Curzio, Compliant alkali silicate sealing glass for solid oxide fuel cell applications: Thermal cycle stability and chemical compatibility Journal of Power Sources 196 (2011) 2709–2716.

[21] A.F. Gualtieri, Accuracy of XRPD QPA using the combined Rietveld–RIR method, J. Appl. Cryst. 33 (2000) 267–278.

[22] W.A. Dollase, Correction of intensities for preferred orientation in powder diffractometry: application of the March model, J. Appl. Cryst. 19 (2006) 267–72.

[23] A. Hrubý, Evaluation of glass-forming tendency by means of DTA, Czechoslov. J. Phys. B, 1972, 22, 1187-1193.

[24] A. Dietzel, “Glass structure and glass properties”, Glasstech. Berl. 22 (1968), 41-50

[25] H.E. Kissinger, Variation of peak temperature with heating rate in differential thermal analysis, J. Res. Natl. Bur. Stand. 57 (1956), 217-221.

[26] K. Matusita, S. Sakka, Kinetic study on non-isothermal crystallization of glass by thermal analysis, Bull. Inst. Chem. Res., Kyoto University 59 (1981), 159-171.

[27] T. Ozawa, Kinetics of non-isothermal crystallization, Polymers 12 (1971), 150;

[28] J.W. Christian, The theory of transformations in metals and alloys, Pergamon Press, Oxford, 1965.

[29] A.A. Francis, R.D. Rawlings, R. Sweeney, A.R. Boccaccini, Crystallization kinetic of glass particles prepared from a mixture of coal ash and soda-lime cullet glass, Journal of Non-Crystalline Solids 333 (2004), 187–193.

[30] A. Karamanov, I. Avramov, L. Arrizza, R. Pascova, I. Gutzow, Variation of Avrami parameter during non-isothermal surface crystallization of glass powders with different sizes, J. Non-Cryst. Solids, 358 (2012), 1486–1490

[31] A. Costantini, G. Luciani, F. Branda, Thermal and devitrification behavior of CaO-Ga2O-SiO2 glasses, J. Eur. Cer. Soc. 20 (2000), 1403-1407.

[32] A.G. Sabato, M. Salvo, A. De Miranda, F. Smeacetto, Crystallization behaviour of glass-ceramic sealant for solid oxide fuel cells, Mater. Lett. 141 (2015), 284-287.

[33] M. Erol, S. Kucukbayrak, A. Ersoy-Mericboyu, The application of differential thermal analysis to the study of isothermal and non-isothermal crystallization kinetics of coal fly ash based glasses, J. Non-Cryst. Solids. 355 (2009), 569-576.

[34] E. Bernardo, G. Scarinici, E. Edme, U. Michon, N. Planty, Fast Sintered Gehlenite Glass-Ceramics from Plasma-Vitrified Municipal Solid Waste Incinerator Fly Ashes, J. Am. Ceram. Soc. 92 (2009), 528–530.

[35] Z. Yang, G. Xia, M.S. Walker, C. Whang, J.W. Stevenson, P. Singh, High temperature oxidation/corrosion behaviour of metals and alloys under a hydrogen gradient, Int. J. Hydrogen Energy 32 (2007), 3770-3777.

[36] R. Amendola, P. Gannon, B. Ellingwood, K. Hoyt, P. Piccardo, P. Genocchio, Oxidation behavior of coated and preoxidized ferritic steel in single and dual atmosphere exposures at 800 °C, Surf. Coat. Technol. 206 (2012), 2173-2180.

[37] M. Bram, L. Niewolak, N. Shah, D. Sebold, H. P. Buchkremer, Interaction of sealing material mica with interconnect steel for solid oxide fuel cells application at 600 °C, J. Power Sources 196 (2011), 5889-5896.